

Integration of Periodic, Sub-wavelength Structures in Silicon-on-Insulator Photonic Device Design

Yannick D'Mello^{1*}, Orad Reshef², Santiago Bernal¹, Eslam El-fiky^{1,3}, Yun Wang¹,
Maxime Jacques¹ and David V. Plant¹

¹ Department of Electrical and Computer Engineering, McGill University, H3E 0E9, Montreal, Canada

² Department of Physics, University of Ottawa, K1N 6N5, Ottawa, Canada

³ Department of Electrical Engineering, Alexandria University, 21544, Alexandria, Egypt

* Corresponding author: Yannick.DMello@mail.McGill.ca

Abstract: Rapid advances in high-resolution chip lithography have accelerated nanophotonic device development on the Silicon-on-Insulator (SOI) platform. The ability to create sub-wavelength features in silicon has attracted research in photonic band and dispersion engineering and consequently made available a wide array of device functionalities. By drawing on recent demonstrations, we review how periodic, sub-wavelength structures are used for passive wave manipulation in SOI device design. The optical response is evaluated for both orthogonal polarizations at the telecom wavelengths of 1310 nm and 1550 nm. The results offer a versatile toolkit for the integration of these features in conventional nanophotonic device geometries. Notable benefits include a fine control of dispersion, wavelength and polarization selectivity, and broadband performance.

1 Introduction

Modern technology relies on the internet for data exchange, research, media, and correspondence. As more nodes come online for longer each day, an increased usage of telecommunication networks has placed commensurate demands on the infrastructure supporting online activities. This demand has motivated a shift to higher frequencies in the electromagnetic spectrum. In pursuit of lower latency, reduced propagation loss, energy efficiency, and higher bitrates, transmission lines in the global network have been upgraded to optical fibres [1]. At nearly every scale, from intercontinental submarine cables to intra-datacentre links, communication signals are transmitted at the infrared wavelengths of 1310 nm (O-band) and 1550 nm (C-band) corresponding to the minimum dispersion and loss wavelengths in silica optical fibres [2]. At the transceiver nodes, signal processing is carried out by opto-electronic circuits that interface with electronics hardware. Recent advances in microfabrication and full-wave simulation techniques have boosted on-chip opto-electronic device design using suitable materials. III-V semiconductors including Indium Phosphide (InP), Aluminium Gallium Arsenide (AlGaAs), and Gallium Nitride (GaN), as well as Silicon Nitride (SiN), are heavily used in lasers, detectors, and gain media although device fabrication is limited by price, scalability, and compatibility. They are complemented by the Silicon-on-Insulator (SOI) platform, which uses silicon (Si) as the waveguiding core surrounded by a silicon dioxide (SiO₂) cladding. SOI fabrication leverages mature techniques from the Complementary Metal-Oxide-Semiconductor (CMOS) industry [3] to provide low-loss, cost-effective, mass manufacturable chip production. Its CMOS compatibility makes it highly valuable to opto-electronic telecommunications infrastructure [4, 5]. This immediate application has boosted transceiver development toward increasingly complex device designs at sub-micron resolutions with high scalability [3]. Nowadays, hybrid photonic components comprising integrated circuits from both platforms are routinely incorporated into opto-electronic

products by companies such as Intel, IBM, Ciena, Ericsson, Cisco, and Elenion. These components enable the generation, manipulation, and detection of light with improvements in speed, size, bandwidth, and power consumption.

Si opto-electronic integrated circuits are manufactured using deep ultraviolet lithography (DUVL). The technique enables complex chip architectures that require metallization, doping, heating, multi-etching, and parallel exposure for simultaneous chip fabrication. However, the lithography resolution is low [6] and the lead time takes several months. These limitations present an opportunity for a quicker method of optical device development, the results of which could inform the large scale, complex device designs in DUVL that include opto-electronic control infrastructure. In the research and development phase, electron beam lithography (EBL) is often used due to its relatively short lead time and high lithography resolution [7, 8]. These advantages of EBL have lowered the barrier to entry for passive photonic device development in SOI. Moreover, its high resolution has facilitated novel methods of photonic band engineering using sub-wavelength features. A limitation of EBL is the scalability of chip fabrication via serial exposure, which restricts its application to development environments. In the future, extreme UVL [9] might offer another option to this predicament.

Silicon photonic (SiP) technology exploits the high refractive index contrast and mature fabrication processes of the SOI platform at telecommunication wavelengths. Although the absorption of bulk Si is negligible in this range [10], SOI waveguides still exhibit propagation losses in wafer-level photonic circuitry [11]. Attenuation is mainly caused by scattering due to fabrication imperfections such as lithographic smoothing, sidewall roughness, and mask misalignment [12]. It is compensated to some extent by the high index contrast between Si and SiO₂, which enables smaller devices and waveguide bends, and subsequently denser circuitry [4]. However, their size is still limited because increasing the overlap between confined light and the Si sidewalls contributes further to scattering as seen in Bragg

gratings [12], slot waveguides [13], and directional couplers [14]. In this sense, device performance is dependent on lithography resolution. This suggests that designs incorporating sub-wavelength features would be extremely lossy due to the number of small etch boundaries that interact with light. On the contrary, sub-wavelength gratings (SWG) only weakly interact with confined light [15] and their loss profile is comparable to bulk designs. Such structures have been integrated in waveguides [13], surface [16-18] and edge [19, 20] fibre-chip couplers, directional couplers [21], and polarization [22, 23] and power splitters [24].

Sub-wavelength features that have been incorporated in different devices exhibit similar geometries [25-28]. These similarities allude to a set of guidelines for sub-wavelength engineering in SiP. The transition from bulk Si to sub-wavelength structures is reinforced by fundamental concepts in photonic band engineering. Hence in this work, we present an analysis of state-of-the-art sub-wavelength-based device designs from the perspective of their photonic band structure. In Section 2, we explain concepts in band engineering that are necessary to understand the influence of sub-wavelength features on optical behaviour such as coupling, changing momentum, and pulse distortion. In Section 3, these concepts are applied to single-mode waveguides that employ diffraction, reflection, and propagation as device functionalities. These include diffraction from surface grating couplers and zero-index metamaterials; reflection, resonance, and slow light propagation due to periodic corrugations and holes; and finally, propagation in the sub-wavelength regime directed by the anisotropic propagation constants of SWGs [29]. We extend this analysis in Section 4 to multimode waveguides that have been applied to power and polarization splitters. In Section 5, we investigate instances of sub-wavelength, pseudo-periodic features that appear in designs generated by agnostic optimization techniques such as natural evolution, inverse design, and machine learning. These techniques produce devices with excellent performance, but with complex operating principles that cannot yet be explained, which reinforces the importance of band engineering in SiP design. Finally, we present our concluding remarks in Section 6. Although the scope of this review is limited to the SOI platform, the designs can be transposed other platforms by simply modifying the materials and dimensions appropriately [30].

2 Implications of Photonic Band Structure

The colour of light is determined by the energy of its constituent waves or photons. Both the frequency and wavelength of a wave quantify its energy. In vacuum, the frequency f is inversely proportional to wavelength λ_0 with the proportionality constant being the speed of light c . Inside a material, this relationship is scaled by the refractive index,

$$f = \frac{c}{\lambda_0} = \frac{c}{n(f) \cdot \lambda} = \frac{n(f) \cdot v_p}{\lambda_0} \quad (1)$$

Here v_p is the phase velocity and λ is the wavelength of light inside a material. The spectrally dependent refractive index $n(f)$ specifies the relative velocity of a wavefront at a given frequency. The direction of propagation of a wavefront is described by the direction of its wave vector \vec{k} , which is inversely proportional to the wavelength λ . The propagation speed of the wavefront inside a pulse is given by its phase velocity v_p whereas the pulse energy envelope travels at its

group velocity v_g . The group index n_g scales the group velocity to the speed of light in vacuum. The spectral dependence of either index is the basis of dispersion.

Dispersion is a measure of the spread of a pulse in time and space during propagation. The dispersion relation of a material describes its optical properties and consequently, its spectrally selective interactions with light. This implies that frequency and wavelength are coupled when accounting for dispersion. In conventional materials, $n(f) > 1$ meaning the waves travel slower and with compressed wavelengths. For a heterogeneous mixture of materials, its optical response depends on the spatial distribution of each refractive index. Interestingly, an ordered, periodic distribution of refractive indices has an unconventional optical response for certain frequencies. The nature of this interaction is controlled by the relationship between the optical periodicity of the material and the effective wave vector of the wave [30].

2.1 Periodicity and Wave Vector

A wave can be described by its spatial and temporal frequency. Its temporal frequency f is proportional to the angular frequency ω and its spatial frequency is the wavenumber k that is inversely proportional to λ . The direction of the wave vector \vec{k} provides a valuable degree of freedom in modifying the effective wavenumber with respect to a surface or interface. By controlling the angle of incidence of the wavefront, the projection of its wave vector onto the surface can be appropriately selected [31]. This directionality allows each frequency to be associated with a range of wavenumbers. For example, the refractive indices of Si and SiO₂ are 3.48 and 1.44 respectively, at a frequency f of 193.41 THz [32]. As per equation (1), a wavelength λ_0 of 1550 nm in vacuum or free space would be compressed to a λ of 1076.4 nm in glass and to 445.4 nm in bulk Si. This means that 193.41 THz light propagating through the SOI cladding layer can only be phase-matched with the same frequency in Si if the two waves propagate at an angle of 65.56° with respect to each other. This is depicted in Fig. 1(a) where the phases of both waves are matched, as represented by their wavefronts. The two lowest order modes, shown in Fig. 1(b), are typically utilized in SOI designs to maintain high confinement with a small device footprint.

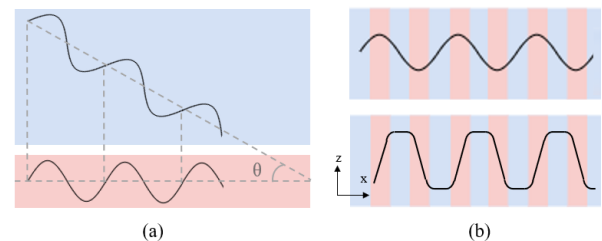


Fig. 1. (a) Two waves of the same frequency in a low (blue) and high (red) refractive index material, and at an angle of θ with respect to each other. The wavefronts (dashed, grey) indicate that the waves are phase-matched at this angle. (b) Electric field distributions of the fundamental (top) and first order (bottom) modes in a grating [30].

The relationship between frequency and wavenumber inside a material is a function of its refractive index tensor and therefore its orientation and geometry. Any geometric modifications are therefore equivalent to a spatial

perturbation of the refractive index. At the sub-wavelength scale, these modifications influence the effective index n_{eff} experienced by propagating light. In this manner, the optical properties of a material can be tailored simply by rearranging its spatial distribution within its surrounding environment. Moreover, imposing a periodicity on these modifications produces unconventional optical behaviour for light waves of a comparable effective wavelength. Such a structured material is called a photonic crystal (PhC) [33, 34]. It is specified as a grating if the periodicity is one-dimensional (1D) as seen in the inset of Fig. 2. The lattice constant (or pitch) of a periodic index perturbation determines its spectral response. The response can be further tuned via the filling factor (or duty cycle) and scaled by the refractive index. These parameters control the effective optical periodicity of the material. Its spatial frequency thereby offers an additional degree of freedom in controlling optical interactions, which complements the directionality of the wave vector. Hence, in any optical interaction, the effective wavenumber is intimately coupled with the pitch of a material in determining the nature of the interaction. The periodicity of the index perturbation also causes the lines in its dispersion diagram to split into bands.

2.2 Band Diagrams

A sub-wavelength, periodic arrangement of the refractive index gives rise to spectrally selective behaviour that can be modelled from Bloch-Floquet theory [30]. The periodicity in a PhC imposes certain constraints on its interaction with light. The behaviour of light within such a periodically arranged structure may be succinctly described by its photonic band diagram. This diagram describes the nature and probability of optical interactions with the PhC in the parameter space of an optical wave. In other words, every combination of frequency and wave vector that can interact with the PhC is represented as a point on the band diagram. Mathematically, each point represents the properties of a wave that produce a real, continuous, and differentiable solution to the dispersion relation [35]. A set of points forms a curve, or band, which indicates the existence of an optical eigenmode for light to occupy during an interaction. Each band therefore contains all possible (k, ω) combinations of light that exhibit the same electromagnetic field distribution in the PhC specified by the corresponding eigenmode of the band. These modes are referred to as Bloch or Floquet modes since the nature of propagation is determined by the optical periodicity of the PhC similar to regular modes in a bulk material.

An exemplary 1D band diagram of a grating pitch of 500 nm is shown in Fig. 2. The ratio of the width of the core material a to the pitch Λ is defined as the filling factor or duty cycle (DC). For a DC of 0.5 shown in Fig. 2, the core and cladding regions contribute equally to the overall optical impedance. Since the pitch and wavenumber are coupled in an optical interaction, the spectral position of the gap in the bands is controlled by the pitch. Similarly, the effect of the DC on the band structure can be inferred as a closing of the band gap toward the lower band for a DC > 0.5 and toward the upper band for a DC < 0.5. Also shown in Fig. 2 are regions in the band diagram where light is diffracted, reflected, or propagated depending on the availability and position of bands in its spectral range. Since a SOI device is surrounded by SiO₂ cladding, the light line mapped in this diagram describes the propagation of light in the cladding.

The light cone includes all (k, ω) combinations above a light line. The green bands in the light cone represent modes that can couple to light in the cladding but as a result, typically cannot propagate inside the PhC. The blue bands describe waves propagating as modes in the PhC that experience a higher effective index than the cladding.

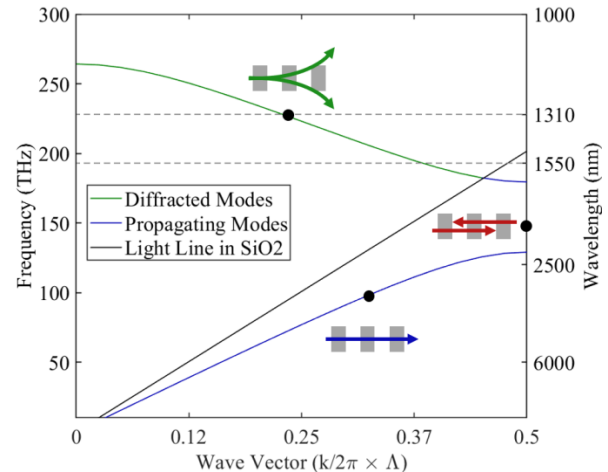


Fig. 2. Band diagram of an SOI grating for the in-plane polarization with a pitch of 500 nm, DC of 0.5, and thickness of 220 nm. The propagation (blue), reflection (red) and diffraction (green) regimes are also shown.

The relationship between the spatial and temporal frequency of an optical wave inside a PhC is mapped by its band diagram. Optical frequencies in the telecommunication range are plotted on the vertical axis. Wave vectors that can be associated with these frequencies are plotted on the horizontal axis as a function of their spatial frequency in relation to the pitch of the PhC. As explained in section 2.1, changing the angle of the wave vector relative to the PhC is equivalent to moving horizontally along the band diagram and selecting a wavenumber. In this context, the phase velocity of a wave is determined simply from its (k, ω) position in the band corresponding to its mode. Its group velocity is the slope of the band at that point.

$$v_p = f\lambda = \frac{\omega}{k}, \quad v_g = \frac{d\omega}{dk} \quad (2)$$

The speed of light in the SiO₂ cladding, for example, is given by the slope of the light line in Fig. 2. The band diagram of a PhC can be used to calculate its coupling efficiency to modes, that is, the probability of light coupling to points on the bands. It therefore indicates the density of optical states accommodated in the PhC as well as the extent and nature of optical interactions. For these reasons, the behaviour of structures presented in this paper will be described in the context of their band diagrams. The band diagrams in this paper were mapped from 3D Finite-Difference-Time-Domain (FDTD) simulations of infinite, planar, 2D PhCs with a Si core thickness of 220 nm and SiO₂ cladding. Spectrally dispersive refractive indices for both materials were used [36]. The TE and TM polarizations were excited by in-plane electric and magnetic dipoles respectively. Bloch periodic boundary conditions were imposed on the in-plane directions of the unit cell while perfectly matching layers were used as the vertical boundaries. Calculations were performed on the first Brillouin zone with the symmetry points labelled as Γ , X,

M, and K depending on the lattice configuration [30]. The intention behind these band diagrams is to provide an intuition for the physical significance of band structure and thereby explain the influence of PhCs on the performance of SOI device designs. There are three distinct regimes of optical interaction that are evident in any band diagram – propagation, reflection, and diffraction.

2.2.1 Propagation

The light line of the cladding imposes an upper bound on the conditions for light confinement. Below the light cone, light waves are confined to the PhC as Bloch modes whose propagation is described by the position and shape of their corresponding bands. A straight band hosts a constant group velocity for optical frequencies that intersect with its region of constant slope. Within this spectral range, a pulse would retain the shape of its energy envelope during propagation. If the intercept of the band is zero, then the phase velocity is equal to the group velocity. An optical pulse within this range would be undistorted because the envelopes and wavefronts of its frequency components would propagate at the same velocity. This region of linear dispersion is the relatively straight section of the lowest band near the Γ point where $k \rightarrow 0$. It is called the sub-wavelength regime [37] because the periodicity of the PhC is smaller than the effective wavelengths interacting with it. As the periodic index perturbations of the PhC are effectively homogenized at this scale, it can be modelled using effective medium theory [38, 39]. The birefringent effective indices n_{\parallel} and n_{\perp} of an infinite, planar SWG can be approximated by Rytov's equations [39],

$$\begin{aligned} n_{\parallel}^2 &= \left(\frac{a}{\Lambda}\right) n_{co}^2 + \left(1 - \frac{a}{\Lambda}\right) n_{cl}^2 \\ \frac{1}{n_{\perp}^2} &= \left(\frac{a}{\Lambda}\right) \frac{1}{n_{co}^2} + \left(1 - \frac{a}{\Lambda}\right) \frac{1}{n_{cl}^2} \end{aligned} \quad (3)$$

Here n_{co} and n_{cl} are the refractive index of the core and cladding respectively. The components n_{\parallel} and n_{\perp} refer to electric field polarization direction being either parallel (propagating in the X direction in Fig. 1) or perpendicular (Z or Y direction in Fig. 1) to the grating lines. A mode in the sub-wavelength regime has a lowered effective index than the core and is therefore higher than the light line of the core. As the index is inversely proportional to velocity, steeper bands due to a lowered group index indicate faster propagation. Along the propagation direction, the width of a SWG can be narrowed to form a waveguide. Sufficiently narrow SWG waveguide widths support delocalized modes [15] since the wavelength is much larger than the pitch. These Bloch modes have a higher group velocity than equivalent modes in a regular waveguide. Additionally, the spectrally insensitive index asserts a uniform response over a broad bandwidth.

2.2.2 Reflection

Taking dispersion into consideration, no propagation occurs for wavelengths that are even integer multiples of the pitch as per the Bragg condition,

$$\lambda = 2mn_{\text{eff}}\Lambda, \quad m = 0, \pm 1, \pm 2 \dots \quad (4)$$

In the Bragg regime, the equivalence of the effective wavelength with the periodicity of a PhC causes forward and backward scattered waves to cancel each other resulting in resonance or reflection. There are no real solutions to the dispersion equation in this range because modes are not supported by the PhC. A corrugated waveguide or SWG in

this regime is called a Bragg grating. Such a PhC only supports standing waves with zero group velocity. An exception to this rule is Dirac-cone based metamaterials where two bands intersect and their homogenization yields a linear dispersion with real, finite group velocities [26].

2.2.3 Diffraction

The light cone of the cladding represents the diffraction or radiation regime. Points above the light line represent light waves that interact with but are not confined to a PhC. These lossy modes are responsible for diffraction and coupling between the PhC and the cladding. For example, the second order mode of the grating in Fig. 2 crosses over the light line resulting in only the larger wavenumbers being confined. In this sense, the grating pitch determines the coupling angle and bandwidth of each diffractive order. The wave vector of light incident on a grating coupler (GC) at an angle θ can be separated into two components – a vertical component k_{\perp} normal to the surface of the GC and a horizontal component k_{\parallel} along the plane of the GC. Light can couple with a GC if the in-plane component k_{\parallel} constructively interferes with the wave vector k_{eff} of confined light in the GC. Mathematically, the difference between the two wave vectors must be an integer multiple of 2π [40],

$$\Delta k_{\text{eff}} - \Delta k_{\parallel} = 2\pi m, \quad m = 0, \pm 1, \pm 2 \dots \quad (5)$$

Under this condition, the incident and confined wave vectors are phase matched, allowing for energy to be transferred between the two waves as depicted in Fig. 1 (a). The above equation can also be interpreted as the grating imparting a $2\pi/\Lambda$ change in momentum to an incident wave. In this sense, the periodicity of the grating allows access to wave vectors outside the first Brillouin zone of the lattice by translating them. When the k-vector of a scattered wave is outside this zone, it is mathematically transformed to a vector inside the zone by the addition or subtraction of reciprocal lattice vectors. This can result in a k-vector with a different direction than the original k-vector. This phenomenon of Umklapp scattering [41] explains the unconventional effect of PhCs on the momentum and direction of light without which it would appear that momentum was not conserved. In the reverse direction, confined light propagating as k_{eff} in the plane of a GC is diffracted at angles that permit constructive interference between the waves radiating from the interface discontinuity of each period in the GC. Assuming k_{\parallel} exists in the cladding, the diffraction angle of the m^{th} order is,

$$\sin \theta = \frac{n_{\text{eff}} - \frac{m\lambda}{a}}{n_{\text{cl}}}, \quad m = 0, \pm 1, \pm 2 \dots \quad (6)$$

The first order $m = 1$ is typically used due to its practical accessibility and coupling efficiency. Note that the k_{\perp} component is directly incident on the GC at an angle of 0° corresponding to the Γ point on the band diagram. As it does not play a role in coupling, it exerts a force on the grating [42]. The Bloch-Floquet mode in this regime is lossy, which is a necessity for coupling to free space due to reciprocity considerations. In Section 3, these concepts will be further examined in the context of single-mode waveguides and their application to device functionalities.

3 Single-Mode Devices

A periodic refractive index distribution gives rise to unconventional optical phenomena such as slow light,

resonance, diffraction, and lossless propagation [43-45]. We now evaluate these phenomena from the perspective of their influence on a fundamental building block, that is, a single etch, single-mode waveguide in which propagation can be analysed almost exclusively. By imposing periodic geometric, or equivalently, index perturbations onto single-mode, strip waveguides, we can interrogate the behaviour of confined wave propagation almost independently of interference, phase modulation, or absorption effects. The approach therefore directly informs the design of surface grating couplers and zero index metamaterials in the diffraction regime, Bragg gratings and PhC nanocavity waveguides in the resonance regime, and edge couplers and SWG waveguides in the sub-wavelength regime.

3.1 SOI Waveguide with Periodic Corrugations

The SOI platform hosts Si waveguides in an SiO₂ cladding with corresponding refractive indices of $n_{\text{core}} \approx 3.48$ and $n_{\text{clad}} \approx 1.44$ respectively [12], within the telecommunication wavelength range. Since the effective wavelength λ_{eff} for a waveguide mode depends on the index [15], this restricts the cross-sectional dimensions to approximately 500 nm along the axes transverse to the propagation direction. A narrower width would reduce modal confinement and prevent guiding, as well as increase sidewall scattering losses. However, the typical thickness of Si crystal growth on a buried oxide (BOX) layer is only 220 nm [46]. This fails to confine the out-of-plane, transverse magnetic (TM) polarizations which instead propagate through the cladding. Only the in-plane, transverse electric (TE) modes are properly confined to the 500 nm width albeit with different effective indices than TM. The fundamental mode profiles for TE and TM polarized light in a standard SiP waveguide are shown in Fig. 3. This effective birefringence in Si waveguides highlights the need for polarization diversity in SiP circuits [47] despite Si being negligibly birefringent.

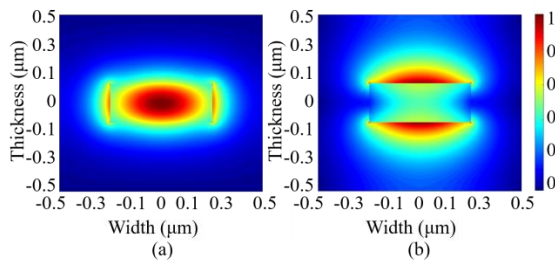


Fig. 3. Cross-sectional profiles of the magnitude of the electric field component of the fundamental (a) TE and (b) TM modes confined to a Si waveguide with a thickness of 220 nm and a width of 500 nm surrounded by SiO₂ cladding.

As the TM mode profile overlaps much less than TE with the waveguide cross-section, it is less susceptible to geometric perturbations or sub-wavelength features present in the waveguide [15]. Fig. 4 shows an exemplary 1D band diagram for a Si waveguide with periodic corrugations along its sidewall at different depths and a pitch Λ of 210 nm. The duty cycle was maintained at 0.5, setting the corrugation width equal to the spacing between successive corrugations.

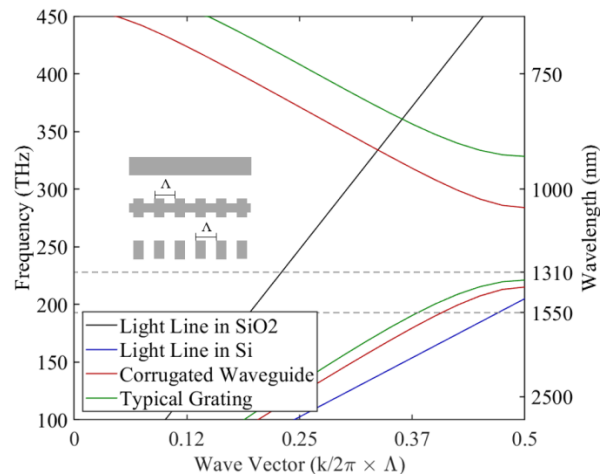


Fig. 4. Band diagram of a corrugated waveguide (red, and middle inset) and grating (green, and bottom inset) with a pitch of 210 nm and DC of 0.5. The light lines of the cladding (black) and core (blue) are also shown.

As illustrated in the insets of Fig. 4, a strip waveguide (of width 500 nm) has a corrugation depth of 0 nm. A depth of 125 nm is commonly used as a frequency filter, and a depth of 250 nm completely etches the core, leaving behind periodically spaced pillars. For long wavelengths, the latter two cases permit light propagation as Bloch modes despite being discontinuous with scattering boundaries. A gap between the bands is caused when the periodicity of the index perturbations fulfills the Bragg condition. Since the corrugations reduce the contribution of Si to the lower index segments of the grating, the overall effective index is lowered causing the bands to shift upward indicating higher propagation velocities and longer effective wavelengths. Deepening the corrugations increases the effective index difference between the corrugated and normal segments thereby widening the gap further. As the energy density of the mode corresponding to the second band is concentrated in the corrugated, lower index region [30], as shown in Fig. 1(b), a deeper corrugation would relatively increase the energy of the system and consequently, its associated phase velocity. In this way, the corrugation depth and fill factor can be used to raise or lower the bands.

3.2 Diffraction Coupling

When the pitch of a grating is larger than the effective wavelength of confined light, scattering occurs at the mismatched impedance boundaries. Although scattering at an interface discontinuity is isotropic, the periodicity of the grating exerts restrictions on scattering in the form of angles of constructive and destructive interference. These angular regions map out the diffraction orders of the grating, which are the higher order modes within the light cone of the band diagram. Normally, only the lower diffraction orders are harnessed in surface fibre-chip GCs. The band structure of a SOI grating pitch of 400 nm is shown in Fig. 5 where both telecom wavelengths couple to the grating modes at different k -vectors [16] but only the O-band is diffracted.

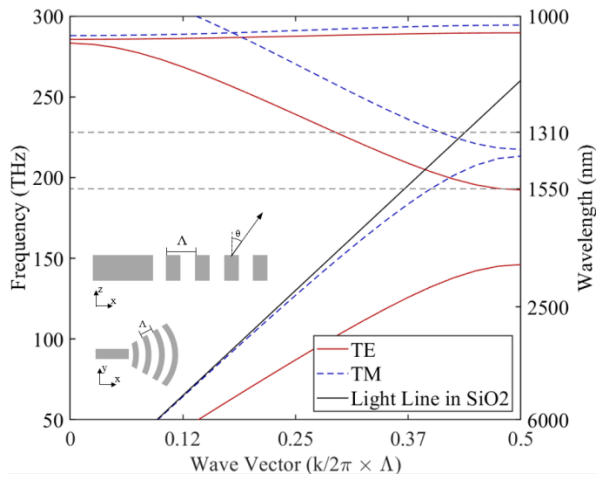


Fig. 5. Band diagram of a SOI grating for TE (solid red) and TM (dashed blue) light with a pitch of 400 nm and DC of 0.5. The insets show a (top) profile view and (bottom) top-down view of its implementation in a GC.

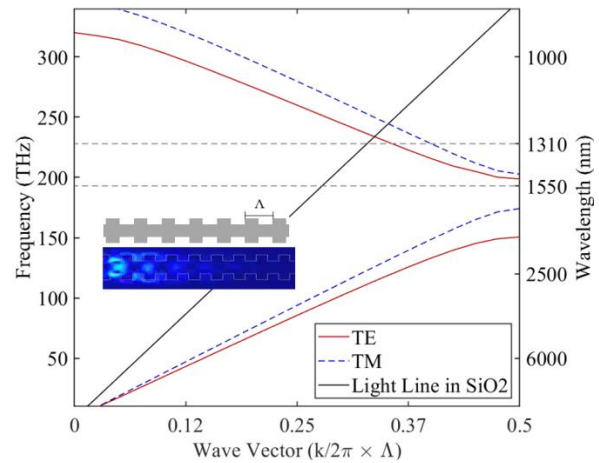
Grating couplers in the SOI platform normally have a large pitch of around 900 nm to access modes above the light line (upper bands in Fig. 5) from within the telecom frequency range so that incident light can couple from free space. Due to their large pitch requirement, and consequently large feature sizes, GC resolutions are typically CMOS-compatible. Most designs utilize a lower effective index difference between the alternating sections of the grating to optimize the coupling efficiency and bandwidth by easing the transition to free space. This is achieved by increasing the cladding index through partial etches or sub-wavelength structures that draw on concepts in effective medium theory [38, 39]. Designs using 2D PhCs [48-51] also offer polarization, mode, and frequency selective functionalities.

Recently, the realization of on-chip, zero-index metamaterials [52] has introduced a new regime of radiation that is emitted transverse to the direction of propagation of a waveguide in both the in-plane and out-of-plane directions. Analogous to the electric band structure in graphene, this phenomenon was made possible by a Dirac cone at the Γ ($k=0$) point of a PhC [53]. A Dirac cone is a band-crossing that exhibits linear dispersion (constant group velocity) in both bands for frequencies near the crossing. The position of the bands in the Brillouin zone gives rise to an infinite phase velocity and wavelength. Using the lattice parameters of the PhC, its spectral position can be aligned to frequencies within the telecom wavelength range. This has recently been realized in CMOS-compatible feature sizes on the SOI platform [54, 55]. Radiation modes can also be excited transverse to the axis of a zero-index metamaterial waveguide resulting in far-field directional couplers [14] and other phenomena [26, 56].

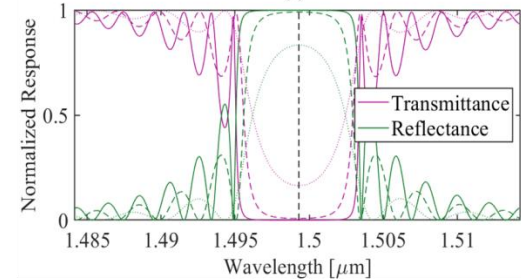
3.3 Bragg Reflection

Arguably the most recognizable diffraction element in guided wave optics, Bragg gratings operate as band-stop filters [57-59]. The extent of Bragg reflection can be tuned to either reflect, transmit, or slow down light thereby inducing a resonant effect along the length of the grating. Fig. 6 shows the band diagram and the transmission and reflection profiles for a Bragg grating of pitch 300 nm that has a 3-dB bandwidth of 20 nm in the O-band [12]. Note that the band gap for TE

polarized light is larger due to a higher overlap with the waveguide cross-section, as depicted in Fig. 3. Such corrugated waveguides are used as frequency filters or contra-directional couplers [60, 61]. The depth of a Bragg filter is determined by the number of grating periods as well as fabrication fidelity. Resonant effects are prevalent after only a few periods. Lithographic smoothing at the corners of each corrugation reduce the step impedance between sections, which manifests as a reduction in the bandwidth and isolation, as can be seen in the dashed and dotted lines of Fig. 6(b).



(a)



(b)

Fig. 6. (a) Band diagram of a SOI Bragg grating for TE (solid red) and TM (dashed blue) modes with a pitch of 300 nm, DC of 0.5, width of 500 nm, and 125 nm corrugations [12]. The insets show its implementation in (top) a Bragg grating that (bottom) reflects 1550 nm light. (b) Simulated degradation of its optical response (dashed and dotted lines) due to increased lithographic smoothing [12].

In contrast to sidewall corrugations, a periodically varying dielectric permittivity has also been incorporated in waveguides by embedding holes along its axis as seen in Fig. 7. The holes impose a sinusoidally varying effective index that asserts a stopband similar to the Bragg grating. Such PhC waveguides have been used as resonant or slow light cavities [62, 63] and as optomechanical nanobeam cavities [64, 65] for sensing or modulation [66, 67]. In most resonant cavity designs using corrugated sidewalls or axial holes, back-reflections have been minimized by an apodization of the hole diameters [68]. Such a gradually increasing step index difference provides a smoother transition to the step index profile of the resonant waveguide and consequently better overall performance.

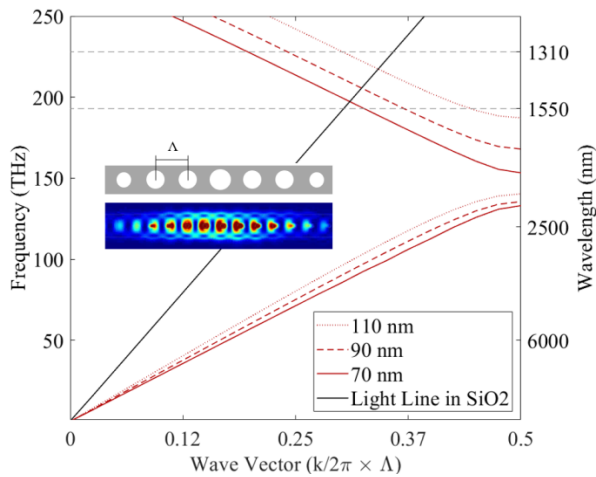


Fig. 7. Band diagram of a SOI square lattice with a pitch of 360 nm and increasing hole diameters of 70 nm (solid), 90 nm (dashed), 110 nm (dotted). The insets show its implementation in (top) a PhC cavity waveguide supporting (bottom) 1550 nm pulse propagation.

Similar to a PhC waveguide, the bandgap in a 2D PhC slab has also been demonstrated in its capacity for waveguiding by introducing a line defect [63, 69]. Such designs exert a high confinement factor on light propagating through the defect, which allows for extremely dense routing with 90° bends [70]. However, as the defect exists within the bandgap of the 2D PhC, the bandwidth supported by a PhC slab waveguide is much lower than regular waveguides. Alternatively, light can also propagate as Bloch modes confined to a waveguide by implementing gratings designed in the sub-wavelength regime.

3.4 Sub-wavelength Propagation

If the pitch of a grating is smaller than the effective wavelength of interacting light, then light may propagate through the PhC as a Bloch mode. Such modes have a low overlap with the sidewalls of the grating, which facilitates relatively low loss, diffraction-less propagation due to negligible scattering from any sidewall roughness [15]. A SWG exhibits anisotropy due to its directional periodicity and can therefore be treated as a uniaxial crystal. The effective index experienced by modes in a SWG-based waveguide depends on the direction of the SWG axis with respect to the polarization direction, as shown in equation (3). In the deep sub-wavelength regime, a SWG can be modeled using effective medium theory [38, 39]. The maximum pitch supported for a SOI SWG waveguide propagating the O and C bands has been demonstrated at around 200 nm [19] as shown in Fig. 8, beyond which the Bragg condition is approached. Individual segments of the grating may be tuned to regulate the mode size or match the effective index in transitioning to a strip waveguide. These parameters have been applied to an edge coupler design with a polarization-independent coupling efficiency of 92% over a 100 nm bandwidth [71]. By reducing the size of individual segments, the effective index was lowered, and the mode size was enlarged to match propagation to a single mode fiber.

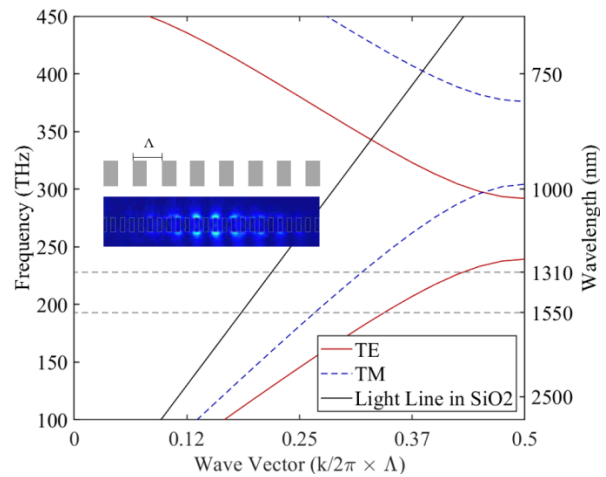


Fig. 8. Band diagram of a SOI SWG for TE (solid red) and TM (dashed blue) polarizations with a pitch of 200 nm and DC of 0.5. The insets show its implementation as (top) a SWG edge coupler [19] supporting (bottom) 1550 nm pulse propagation.

A valuable property of SWGs is their linear dispersion profile at long wavelengths, which translates to a spectrally independent phase velocity and effective index. This property allows SWGs to be used in highly broadband devices covering both the O and C bands. Furthermore, it has been recently demonstrated that such waveguides are extremely tolerant to fabrication imperfections and can support efficient light propagation even across missing or deformed gratings [72]. Note that eliminating a SWG section would be akin to doubling the periodicity at a fill factor of 0.25 albeit for barely 1-2 periods. This effect is inconsequential because the strength of PhC behaviour depends on the number of periods contained by the PhC. A DC of 0.5 is typically maintained for single-etch SWG waveguides to maximize their fabrication tolerance, although dispersion can still be fine-tuned by changing their width, pitch, or tilt.

The laminar, periodic structure of a SWG exhibits similar optical behaviour to a homogeneous, uniaxial crystal [29]. Bloch modes propagating through a SWG are subjected to an anisotropic effective index. For comparison, the effective index of a fundamental, TE polarized Bloch-Floquet mode propagating across a SWG (as seen in Fig. 4 and Fig. 2) is about 2.66 using equation (3), whereas it is 1.88 when traveling along the grating elements [29, 39]. The TM polarization is less influenced by the grating angle because its direction of polarization is always parallel to the interfaces irrespective of its direction of propagation. Indeed, the effective index of the TM mode increases slightly when angled with respect to the grating [29]. Alternatively, it has been shown that the grating angle itself can be tilted in a SWG waveguide thereby modifying the effective index. In such a case, the phase front of the modes is also tilted proportional to the grating [73] and can be determined from their wave vectors using the dispersion equation [29, 35]. This manifestation of tilt in the band diagram of a SWG waveguide requires a treatment of the grating as a periodic, laminar, multilayer stack [30]. The effect can be seen in the 2D band diagram of Fig. 9 for a SWG with a period of 250 nm [29] where a tilt of 45° was demonstrated.

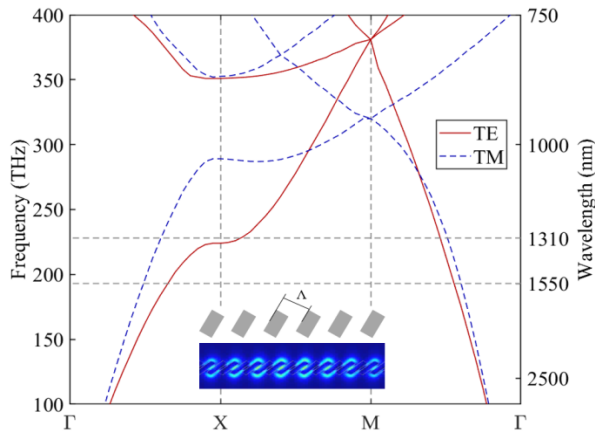


Fig. 9. Band diagram for a SOI SWG for TE (solid red) and TM (dashed blue) polarizations with a pitch of 250 nm and DC of 0.5 [29]. The insets show its implementation in (top) a tilted SWG waveguide supporting (bottom) 1550 nm pulse propagation.

From this perspective, the SWG waveguide can be interpreted as a 2D lattice with the propagation directed by its tilt angle θ . When the angle is increased and pitch Λ is maintained, the effective grating pitch Λ_{eff} along the direction of propagation is increased to $\Lambda \sec \theta$. Decreasing the effective grating vector consequently reduces the energy $\hbar\omega$ required to support modes. In the context of dispersion, the bands are therefore lowered in frequency. Lowering the bands allows access to modes in the X-M region of the crystal reciprocal lattice that were originally in the sub-wavelength regime for a grating tilt of 0° . Conversely, a propagating mode originally available in the Γ -X region now enters the Bragg regime and is instead guided along the tilt direction in the X-M region. In this manner, the grating tilt offers an additional degree of freedom to engineer the effective index albeit at the cost of higher dispersion. The convenience of using the tilt angle as a parameter for passive wave manipulation is that it does not require smaller feature sizes at larger angles. A rather aggrandized extrapolation of this concept that is still within the realm of single mode waveguiding, is a completely tilted SWG with an angle of 90° but only two periods [66]. Although such a design supports lateral light propagation as a slotted light waveguide, it is a different physical phenomenon because of its equivalence to a potential barrier with a thin well in which the pulse is highly confined [74]. The slot offers a strong interaction with its confined mode, which can also be achieved by suspending the SWG albeit for longer wavelengths [75, 76]. Using multiple grating periods allows for homogenization, and across a sufficiently wide cross-section, higher order modes are excited. This has been extensively explored in the context of multi-mode waveguides.

4 Multi-Mode Devices

The fundamental mode profile of confined light in a single mode waveguide can be expanded to any desired width by adiabatically tapering it. A sufficiently gradual taper does not perturb the effective index along the direction of propagation, and therefore retains its mode profiles. On the other hand, a sharp expansion of the waveguide width induces a strong

perturbation of the effective index. In this situation, the fundamental mode leaks energy into higher order modes causing multi-modal propagation. It is analogous to a charged particle traveling across a potential drop. Waveguides that incite and support higher order modes are referred to as multi-mode interferometers (MMI) due to their characteristic interference patterns caused by the superposition of the modes [77]. Antinodes formed at each self-imaging length in the MMI can be extracted as a single mode, and subsequently applied to intensity or polarization splitting. Additionally, the integration of sub-wavelength structures such as SWGs or PhCs in MMI-based device designs has been shown to appreciably improve the insertion loss, extinction ratio, and bandwidth [22, 24, 78].

4.1 Intensity Splitters

A drastic change in waveguide width excites higher order modes of which each propagates with its own propagation constant $\beta = 2\pi n_{\text{eff}}/\lambda$. Their mutual interference produces self-images of the input at beat lengths L_π that depend on the propagation constants of the first two modes β_0 and β_1 [77],

$$L_{\text{SI},p} \rightarrow \frac{p}{2}(3L_\pi) = \frac{3p}{2} \left(\frac{\pi}{\beta_0 - \beta_1} \right) \approx \frac{p}{2} \left(\frac{4W_{\text{eff}}^2 n_{\text{core}}}{\lambda_0} \right) \quad (7)$$

A single image is formed at every even value of p whereas a two-fold image is formed at every odd value. The paraxial approximation for L_π is valid for MMIs with a high refractive index contrast as in the SOI platform. In this case, the effective width W_{eff} can be approximated by the MMI width. As intensity splitters, MMI-based designs have been shown to offer an appreciable bandwidth and fabrication tolerance due to their large cross-section and feature sizes. Additionally, by integrating a SWG into the MMI, its effective index is reduced, thereby shortening the beat length (as calculated from the phase constants) and allowing for smaller designs [78]. As explained in Section 3.4, the linear dispersion of the mode in the sub-wavelength regime also enhances the operating bandwidth tremendously [79]. This point is illustrated in the band diagram of Fig. 10 that shows a constant slope and therefore a constant, reduced effective index across the telecom O and C bands.

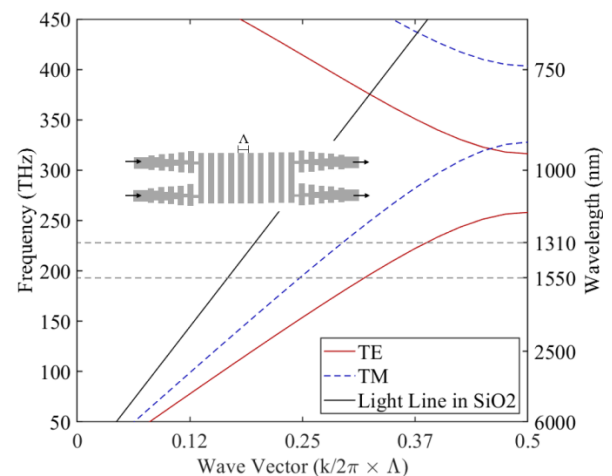


Fig. 10. Band diagram of a SOI SWG for TE (solid red) and TM (dashed blue) polarizations with a pitch of 190 nm and DC of 0.5. The inset shows its implementation in a MMI-based 2×2 intensity splitter [78].

The 2×2 MMI shown in the inset of Fig. 10 demonstrates an equal splitting ratio between both ports over a bandwidth of 300 nm [78]. In such a SWG-based MMI, the beat length in equation (7) is calculated from the propagation constants of the fundamental and first-order Bloch-Floquet modes. The choice of a single or two-fold imaging length depends on the design constraints, such as whether filtering or splitting is required. If a higher splitting ratio is required for applications such as monitoring the power through a waveguide, the same concept may be applied to the design of a variable intensity splitter as shown in Fig. 11. By using a central input and extracting light at the two-fold imaging length, a 1×2 MMI was developed as a power tap for the C-band [80]. In this application, one output could be connected to a photonic integrated circuit with the other to a detector. The splitting ratio was tuned using the device geometry by cutting a corner of the MMI at the side that was designated as the lower power output. Variable splitting ratios were achieved for a 225 nm pitch over a bandwidth of 100 nm [24].

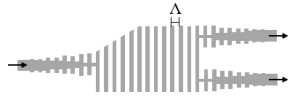


Fig. 11. Integration of a SWG in the design of a 1×2 MMI variable intensity splitter [24].

The broad bandwidth and customizable splitting ratios offered by SWG MMIs lays the basis for SiP transceiver designs that operate across the entire telecommunications spectrum. Evidence of this claim is in the performance enhancements realized for polarization splitters that utilize a PhC or SWG in an MMI-based design.

4.2 Polarization Splitters

An asymmetric waveguide cross-section in the SOI platform causes birefringence due to an inherent effective index difference between the fundamental TE and TM mode profiles as seen in Fig. 3. However, polarization and mode division multiplexing are often incorporated in SiP circuit design. This introduces the need for polarization diversity in SiP circuits, for which polarization splitters are essential. An intuitive solution is to exploit the effective birefringence in SOI devices for polarization discrimination. Similar to the MMI design in Fig. 10, a polarization splitter has been demonstrated [22] with a dual polarization input and separate TE and TM outputs. Using the difference in effective indices, and consequently different beat lengths, a self-image of the input was produced at different propagation lengths for each polarization. As can be inferred from the schematic in Fig. 12, the TE beat length was approximately double that for TM. The integration of a SWG with a pitch of 180 nm into the MMI-based polarization beam splitter (PBS) design broadened its bandwidth to 100 nm.

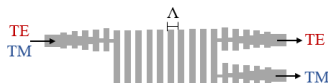


Fig. 12. Integration of a SWG in the design of a PBS based on the 2×2 MMI [22] shown in Fig. 10.

As described in Section 3.3 for SWG design, the grating tilt may be used as an additional parameter for controlling the effective index in a PBS [79]. The grating tilt controls the

structural anisotropy of the device. In doing so, the effective index of the TE polarization can be increased across the spectrum whereas the effective index for TM light is negligibly affected due to its propagation mainly through the SiO₂ cladding. By fine-tuning the tilt parameters to produce the device shown in Fig. 13, the TE self-imaging length was reduced so that the overall device length was shortened to less than 100 μm without compromising on bandwidth or extinction ratio.

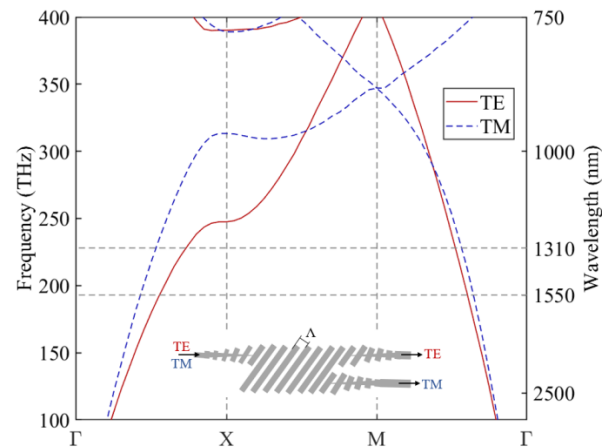


Fig. 13. Band diagram of a SOI SWG for TE (solid red) and TM (dashed blue) polarizations with a pitch of 220 nm and DC of 0.5. The inset shows its integration in the design of a PBS with a 7° tilt [79].

A tilted SWG PBS supports a TE direct image at the same length as the TM mirrored image due to its anisotropy-induced birefringence. This is due to the ratio of the effective indices for propagation directions parallel and perpendicular to the grating elements [78]. In the context of the band diagram in Fig. 13, a higher position of the fundamental TM mode at the X point indicates a higher phase velocity and as such, a lower effective index for TM light propagating across the grating, as well as a higher index of the TM mode propagating along the grating at the M point. This higher ratio between the indices results in a longer beat length for TM light, which also explains the reasoning behind the design in Fig. 12. In this manner, the position of the TE output port can be made to coincide with the location of the TM port along the propagation length. The improved performance suggests that integrating a tilted SWG into an angled MMI PBS design [81] could possibly reduce the form factor further while maintaining the operation bandwidth.

High extinction ratios could also be achieved by filtering the TE polarization at the TM output, as has been shown in [82] and its SiP equivalent [83]. In these designs, a PhC with a triangular lattice was embedded in a conventional MMI as can be seen in the schematic of Fig. 14. The 2D band structure of the PhC opened a bandgap for TE polarized light that was collected as a back-reflection. TM light, however, propagated unhindered in the sub-wavelength regime and was collected at its mirrored self-imaging length.

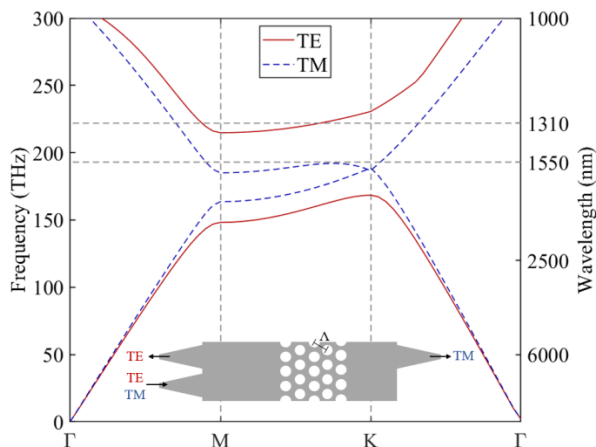


Fig. 14. Band diagram of a PhC for TE (solid red) and TM (dashed blue) polarizations with a 390 nm pitch hosting a triangular lattice of holes of radius of 117 nm. The inset shows its integration in the design of a MMI-based PBS [83].

Note that the devices described in this paper have been selected for the straightforward design approach they employ. Many other sub-wavelength designs have been proposed for polarization splitting [37] such as contra-directional couplers that filter polarizations [61], directional couplers that separate polarizations [14], and polarization rotators [84, 85]. Furthermore, sub-wavelength structures have been incorporated into a number of SiP device designs including Mach-Zehnder interferometers [86], rings [87], switches [88], detectors [89], demultiplexers [90], and lasers [91, 92]. Interestingly, the successful integration of sub-wavelength structures in nanophotonic device design also extends beyond our level of understanding. At this extreme, devices utilizing dispersion engineering have been realized through natural and artificial means by optimizing the geometry directly. These designs meet their performance targets despite a lack of knowledge surrounding the device physics.

5 Extension: Optimized Devices

The application space for sub-wavelength integration in SOI is relatively new with most of the previously mentioned devices having been demonstrated in the last few years. This raises the question of how much further these functionalities can be optimized. We therefore turn our attention to designs generated by state-of-the-art optimization processes.

5.1 Evolution: Natural Selection

Photosynthetic organisms absorb solar energy to activate chemical processes that produce oxygen and drive the carbon cycle. Up to 40% of photosynthetic activity is driven by aquatic phytoplankton called diatoms [93]. More than 150,000 species of diatoms have evolved to thrive in most aquatic habitats. Yet despite their ubiquity, diatoms utilize fairly conventional pigments such as chlorophyll A that offer no apparent advantage to the photosynthetic process [94]. Additionally, their limited motility in the turbulent photic zone indicates a lack of directional orientation toward the sun, which puts them at a significant disadvantage. This is why their proliferation in such circumstances suggests the possibility of a physical mechanism that aids the diatom in

photosynthesis. Indeed, diatoms grow a biosilica shell that hosts a lattice of periodic perforations resembling a 2D PhC [95, 96], which is speculated to assist in light harvesting. Evidence to corroborate this speculation is mounting, such as recent numerical analyses of the band structure of the shell [97] as replicated in Fig. 15 for the *Nitzschia Filiformis* species.

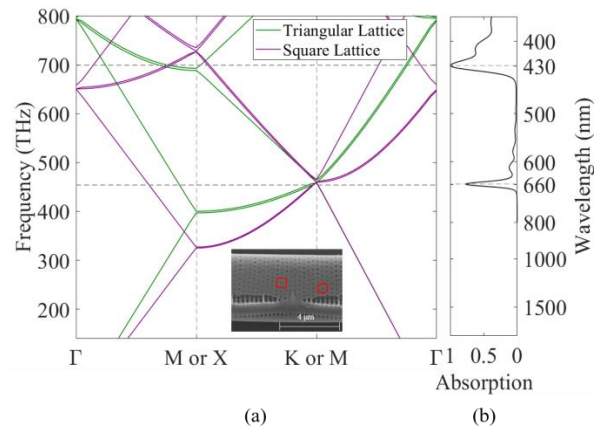


Fig. 15. (a) Band diagram of a biosilica frustule with square (purple) and triangular (green) lattice configurations with pitches of 330 nm and 300 nm respectively, for water holes of 80 nm diameter. (b) The absorption spectrum of chlorophyll A with peaks at 449 nm and 660 nm [98].

An examination of this band structure reveals promising insights into their light harvesting mechanisms. For example, pseudogaps in the band diagram are seen to coincide with the absorption peaks of chlorophyll A. This high density of optical states suggests a slow light effect to compensate for the limited photosynthetic conversion rate of the chloroplasts during periods of heavy illumination. The PhC topography also exhibits a certain level of disorder, which could be interpreted as fabrication imperfections if every species did not exhibit similar topographical disorder. However, the proliferation of diatoms over several millennia of evolution is testament to the level of optimization that they have undergone through selective mutations. We therefore speculate that disorder induces a higher fabrication tolerance by effectively smearing the band structure around the absorption peaks to increase the bandwidth of the pseudogap effect. Similar disorder has been observed in designs that demonstrate an improved fabrication tolerance [72, 87, 99] as compared to regular periodic perturbations. This has been further verified by computational optimization techniques for nanophotonic device design.

5.2 Computational Optimization

An explosive growth in numerical simulations employing nonlinear and topology optimization algorithms has accelerated design principles in many fields [100, 101] of which nanophotonics is no exception. Advanced pattern recognition algorithms using artificial intelligence have produced designs that contain insights beyond known engineering principles. Many categories of these optimization algorithms have been investigated in the context of SiP design optimization. A gradient-based search tests for convergence,

computes a search direction and step length, and then iterates through the parameter space of a device design to improve its performance. A combinatorial search optimizes feasible solutions by eliminating infeasible results. Neural networks on the other hand, use one-time training instances to build and curate a large dataset of examples from which to infer patterns. Although iterative optimization techniques are appreciably more informed than the relatively blind methods of machine learning, both produce informative results. For example, polarization splitters have been realized using inverse design [102, 103] and nonlinear optimization [104] techniques. These methods have produced the MMI-based PBS device designs in Fig. 16, which are similar to those presented in Section 4.2 albeit with the utilization of currently undeveloped mechanisms of dispersion engineering.

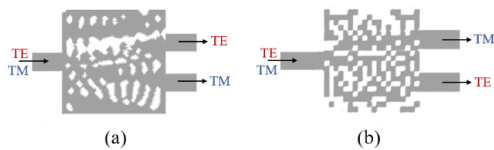


Fig. 16. Schematics of reverse engineered PBS devices with relatively small footprints of (left) $2.8 \times 2.8 \mu\text{m}$ [102], and (right) $2.4 \times 2.4 \mu\text{m}$ [104].

The performance of such devices, despite their compact form factors, are as yet unachievable through known design principles. While such designs demonstrate the value of optimization techniques in generating hitherto unforeseen results, caution must be taken when a device design precedes an understanding of the mechanisms at play in its operation. The value of this process could be seen as providing novel and possibly unintuitive directions for future research.

6 Conclusion

The benefit of combining sub-wavelength structures with nanophotonic devices for dispersion engineering was developed and evaluated. In doing so, we have provided a framework for SiP dispersion engineering in the SOI platform. These guidelines are based on an intuitive understanding of the unique behaviours of modes that reside in different regions of a band diagram. For example, the diffractive regime is used for external coupling; the reflection regime for filters, resonators, and reflectors; and the propagation regime for broadband responses, polarization discrimination, and index tuning. Based on these tools, known concepts in Bloch-Floquet theory have been integrated in conventional geometries. Tactics such as tuning the index in a tilted SWG [29], broadening the bandwidth of an MMI [24, 78], lowering the insertion loss of an edge coupler [71], increasing the coupling range of a directional coupler [14], or widening the extinction ratio in a PBS [82, 83] have improved and expanded device performance. Furthermore, natural and computational optimization techniques have produced specialized, dispersion engineered optical devices that we have yet to completely understand [95, 97, 102, 104]. Be it natural or human-made, these devices suggest new directions for the iterative scientific process to investigate and subsequently develop. With the aid of biomimetics and reverse engineering, the gap between our understanding and our design achievements leaves much to be explored.

7 Acknowledgments

The authors would like to thank Shai Tsesses, Ludwig Krinner, Bradley Siwick, Kathleen McGarvey, and David Patel for advice and feedback. This work is supported by McGill University, the National Science and Engineering Research Council (NSERC) of Canada, the NSERC Collaborative Research and Training Experience (CREATE) Silicon Electronic Photonic Integrated Circuits (SiEPIC) program, and Canadian Microelectronics Corporation (CMC).

8 References

- [1] T. G. Brown, "Optical fibers and fiber-optic communications," *FIBER OPTICS HANDBOOK*, 2002.
- [2] A. Yariv and P. Yeh, *Photonics: Optical Electronics in Modern Communications (The Oxford Series in Electrical and Computer Engineering)*. Oxford University Press, Inc., 2006.
- [3] D. Thomson *et al.*, "Roadmap on silicon photonics," *Journal of Optics*, vol. 18, no. 7, 2016.
- [4] R. Soref and J. Lorenzo, "All-silicon active and passive guided-wave components for $\lambda = 1.3$ and $1.6 \mu\text{m}$," *IEEE Journal of Quantum Electronics*, vol. 22, no. 6, pp. 873-879, 1986.
- [5] N. Abadía *et al.*, "Low-Power consumption Franz-Keldysh effect plasmonic modulator," *Optics Express*, vol. 22, no. 9, pp. 11236-11243, 2014/05/05 2014, doi: 10.1364/OE.22.011236.
- [6] S. Pauliac, S. Landis, J. Foucher, J. Thiault, and O. Faynot, *Hybrid lithography process for nano-scale devices*. 2006, pp. 1761-1766.
- [7] "NanoSOI Design Rules." Applied Nanotools Inc. <https://www.appliednt.com/nanosoi/sys/resources/rules/> (accessed 26 March 2019, 2019).
- [8] L. Chrostowski *et al.*, "Silicon Photonic Circuit Design Using Rapid Prototyping Foundry Process Design Kits," *IEEE Journal of Selected Topics in Quantum Electronics*, pp. 1-1, 2019, doi: 10.1109/JSTQE.2019.2917501.
- [9] B. Wu and A. Kumar, "Extreme ultraviolet lithography: A review," *Journal of Vacuum Science & Technology B: Microelectronics and Nanometer Structures Processing, Measurement, and Phenomena*, vol. 25, no. 6, pp. 1743-1761, 2007/11/01 2007, doi: 10.1116/1.2794048.
- [10] H. Chen, X. Luo, and A. W. Poon, "Cavity-enhanced photocurrent generation by $1.55 \mu\text{m}$ wavelengths linear absorption in a p-i-n diode embedded silicon microring resonator," *Applied Physics Letters*, vol. 95, no. 17, p. 171111, 2009/10/26 2009, doi: 10.1063/1.3257384.
- [11] J. F. Bauters *et al.*, "Planar waveguides with less than 0.1 dB/m propagation loss fabricated with wafer bonding," *Optics Express*, vol. 19, no. 24, pp. 24090-24101, 2011/11/21 2011, doi: 10.1364/OE.19.024090.
- [12] L. Chrostowski and M. Hochberg, *Silicon photonics design: from devices to systems*. Cambridge University Press, 2015.
- [13] Z. Ruan, L. Shen, S. Zheng, and J. Wang, "Subwavelength grating slot (SWGS) waveguide on silicon platform," *Optics express*, vol. 25, no. 15, pp. 18250-18264, 2017.
- [14] O. Reshef, C. Nacke, J. Upham, and R. W. Boyd, "Waveguide-to-waveguide directional coupling beyond a free space wavelength," in *Conference on Lasers and Electro-Optics*, San Jose, California, 2019/05/05 2019: Optical Society of America, in OSA Technical Digest, p. SF1J.6, doi: 10.1364/CLEO_SI.2019.SF1J.6. [Online]. Available: http://www.osapublishing.org/abstract.cfm?URI=CLEO_SI-2019-SF1J.6
- [15] P. J. Bock *et al.*, "Subwavelength grating periodic structures in silicon-on-insulator: a new type of microphotonic waveguide," *Optics Express*, vol. 18, no. 19, pp. 20251-20262, 2010/09/13 2010, doi: 10.1364/OE.18.020251.

- [16] Y. Wang *et al.*, "Compact single-etched sub-wavelength grating couplers for O-band application," *Optics Express*, vol. 25, no. 24, pp. 30582-30590, 2017.
- [17] R. Halir, P. Cheben, S. Janz, D.-X. Xu, Í. Molina-Fernández, and J. G. Wangüemert-Pérez, "Waveguide grating coupler with subwavelength microstructures," *Optics Letters*, vol. 34, no. 9, pp. 1408-1410, 2009/05/01 2009, doi: 10.1364/OL.34.001408.
- [18] X. Chen and H. K. Tsang, "Nanoholes Grating Couplers for Coupling Between Silicon-on-Insulator Waveguides and Optical Fibers," *IEEE Photonics Journal*, vol. 1, no. 3, pp. 184-190, 2009, doi: 10.1109/JPHOT.2009.2031685.
- [19] M. Papes *et al.*, "Fiber-chip edge coupler with large mode size for silicon photonic wire waveguides," *Optics express*, vol. 24, no. 5, pp. 5026-5038, 2016.
- [20] P. Cheben, D. X. Xu, S. Janz, and A. Densmore, "Subwavelength waveguide grating for mode conversion and light coupling in integrated optics," *Optics Express*, vol. 14, no. 11, pp. 4695-4702, 2006/05/29 2006, doi: 10.1364/OE.14.004695.
- [21] Y. Wang *et al.*, "Compact broadband directional couplers using subwavelength gratings," *IEEE Photonics Journal*, vol. 8, no. 3, pp. 1-8, 2016.
- [22] L. Xu *et al.*, "Polarization beam splitter based on MMI coupler with SWG birefringence engineering on SOI," *IEEE Photon. Technol. Lett.*, vol. 30, no. 4, pp. 403-406, 2018.
- [23] N. Abadía *et al.*, "CMOS-compatible multi-band plasmonic TE-pass polarizer," *Optics Express*, vol. 26, no. 23, pp. 30292-30304, 2018/11/12 2018, doi: 10.1364/OE.26.030292.
- [24] E. El-Fiky *et al.*, "Ultra-Broadband and Compact Asymmetrical Beam Splitter Enabled by Angled Sub-Wavelength Grating MMI," in *Conference on Lasers and Electro-Optics*, San Jose, California, 2018/05/13 2018: Optical Society of America, in OSA Technical Digest (online), p. STh4A.7, doi: 10.1364/CLEO_SI.2018.STh4A.7. [Online]. Available: http://www.osapublishing.org/abstract.cfm?URI=CLEO_SI-2018-STh4A.7
- [25] P. Cheben, R. Halir, J. H. Schmid, H. A. Atwater, and D. R. Smith, "Subwavelength integrated photonics," *Nature*, vol. 560, no. 7720, pp. 565-572, 2018/08/01 2018, doi: 10.1038/s41586-018-0421-7.
- [26] D. I. Vulis, O. Reshef, P. Camayd-Muñoz, and E. Mazur, "Manipulating the flow of light using Dirac-cone zero-index metamaterials," *Reports on Progress in Physics*, vol. 82, no. 1, p. 012001, 2018/11/05 2018, doi: 10.1088/1361-6633/aad3e5.
- [27] W. Zhou, Z. Cheng, X. Chen, K. Xu, X. Sun, and H. Tsang, "Subwavelength Engineering in Silicon Photonic Devices," *IEEE Journal of Selected Topics in Quantum Electronics*, vol. 25, no. 3, pp. 1-13, 2019, doi: 10.1109/JSTQE.2019.2899757.
- [28] I. Staude and J. Schilling, "Metamaterial-inspired silicon nanophotonics," *Nature Photonics*, Review Article vol. 11, p. 274, 04/28/online 2017, doi: 10.1038/nphoton.2017.39.
- [29] J. M. Luque-González *et al.*, "Tilted subwavelength gratings: controlling anisotropy in metamaterial nanophotonic waveguides," *Optics Letters*, vol. 43, no. 19, pp. 4691-4694, 2018/10/01 2018, doi: 10.1364/OL.43.004691.
- [30] J. D. Joannopoulos, S. G. Johnson, J. N. Winn, and R. D. Meade, *Photonic Crystals: Molding the Flow of Light*, 2 ed. Princeton University Press, 2008.
- [31] E. C. Regan *et al.*, "Direct imaging of isofrequency contours in photonic structures," *Science Advances*, vol. 2, no. 11, p. e1601591, 2016, doi: 10.1126/sciadv.1601591.
- [32] H. H. Li, "Refractive index of silicon and germanium and its wavelength and temperature derivatives," *Journal of Physical and Chemical Reference Data*, vol. 9, no. 3, pp. 561-658, 1980, doi: 10.1063/1.555624.
- [33] S. John, "Strong localization of photons in certain disordered dielectric superlattices," *Physical Review Letters*, vol. 58, no. 23, pp. 2486-2489, 06/08/ 1987, doi: 10.1103/PhysRevLett.58.2486.
- [34] E. Yablonovitch, "Inhibited Spontaneous Emission in Solid-State Physics and Electronics," *Physical Review Letters*, vol. 58, no. 20, pp. 2059-2062, 05/18/ 1987, doi: 10.1103/PhysRevLett.58.2059.
- [35] P. Yeh, A. Yariv, and C.-S. Hong, "Electromagnetic propagation in periodic stratified media. I. General theory*," *J. Opt. Soc. Am.*, vol. 67, no. 4, pp. 423-438, 1977/04/01 1977, doi: 10.1364/JOSA.67.000423.
- [36] E. D. Palik, *Handbook of optical constants of solids*. Academic press, 1998.
- [37] R. Halir *et al.*, "Waveguide sub - wavelength structures: a review of principles and applications," *Laser & Photonics Reviews*, vol. 9, no. 1, pp. 25-49, 2015.
- [38] S. Berthier and J. Lafait, "Effective medium theory: Mathematical determination of the physical solution for the dielectric constant," *Optics Communications*, vol. 33, no. 3, pp. 303-306, 1980/06/01/ 1980, doi: [https://doi.org/10.1016/0030-4018\(80\)90249-7](https://doi.org/10.1016/0030-4018(80)90249-7).
- [39] S. M. Rytov, "Electromagnetic Properties fo a Finely Stratified Medium," *JETP*, vol. 2, 3, pp. 466-475, 1956.
- [40] M. L. Dakss, L. Kuhn, P. F. Heidrich, and B. A. Scott, "Grating Coupler for Efficient Excitation of Optical Guided Waves in Thin Films," *Applied Physics Letters*, vol. 16, no. 12, pp. 523-525, 1970/06/15 1970, doi: 10.1063/1.1653091.
- [41] S. Yamaguti, J.-i. Inoue, O. Haerberlé, and K. Ohtaka, "Photonic crystals versus diffraction gratings in Smith-Purcell radiation," *Physical Review B*, vol. 66, no. 19, p. 195202, 11/07/ 2002, doi: 10.1103/PhysRevB.66.195202.
- [42] G. A. Swartzlander, "Radiation pressure on a diffractive sailcraft," *J. Opt. Soc. Am. B*, vol. 34, no. 6, pp. C25-C30, 2017/06/01 2017, doi: 10.1364/JOSAB.34.000C25.
- [43] Q. Zhao, J. Zhou, F. Zhang, and D. Lippens, "Mie resonance-based dielectric metamaterials," *Materials Today*, vol. 12, no. 12, pp. 60-69, 2009/12/01/ 2009, doi: [https://doi.org/10.1016/S1369-7021\(09\)70318-9](https://doi.org/10.1016/S1369-7021(09)70318-9).
- [44] N. Yu and F. Capasso, "Flat optics with designer metasurfaces," *Nature Materials*, Review Article vol. 13, p. 139, 01/23/online 2014, doi: 10.1038/nmat3839.
- [45] P. Camayd-Muñoz *et al.*, "Lossless Integrated Dirac-Cone Metamaterials," in *Conference on Lasers and Electro-Optics*, San Jose, California, 2016/06/05 2016: Optical Society of America, in OSA Technical Digest (online), p. JW2A.24, doi: 10.1364/CLEO_AT.2016.JW2A.24. [Online]. Available: http://www.osapublishing.org/abstract.cfm?URI=CLEO_AT-2016-JW2A.24
- [46] D. Xu *et al.*, "Silicon Photonic Integration Platform—Have We Found the Sweet Spot?," *IEEE Journal of Selected Topics in Quantum Electronics*, vol. 20, no. 4, pp. 189-205, 2014, doi: 10.1109/JSTQE.2014.2299634.
- [47] T. Barwicz *et al.*, "Polarization-transparent microphotonic devices in the strong confinement limit," *Nature Photonics*, vol. 1, no. 1, p. 57, 2007.
- [48] M. Streshinsky *et al.*, "A compact bi-wavelength polarization splitting grating coupler fabricated in a 220 nm SOI platform," *Optics Express*, vol. 21, no. 25, pp. 31019-31028, 2013/12/16 2013, doi: 10.1364/OE.21.031019.
- [49] E. Schelew, G. W. Rieger, and J. F. Young, "Characterization of Integrated Planar Photonic Crystal Circuits Fabricated by a CMOS Foundry," *Journal of Lightwave Technology*, vol. 31, no. 2, pp. 239-248, 2013/01/15 2013. [Online]. Available: <http://jlt.osa.org/abstract.cfm?URI=jlt-31-2-239>.
- [50] Y. Ohtera, T. Onuki, Y. Inoue, and S. Kawakami, "Multichannel Photonic Crystal Wavelength Filter Array for Near-Infrared Wavelengths," *Journal of Lightwave Technology*, vol. 25, no. 2, pp. 499-503, 2007/02/01 2007. [Online]. Available: <http://jlt.osa.org/abstract.cfm?URI=jlt-25-2-499>.

- [51] W. Zhou and H. K. Tsang, "Dual-wavelength-band subwavelength grating coupler operating in the near infrared and extended shortwave infrared," *Optics Letters*, vol. 44, no. 15, pp. 3621-3624, 2019/08/01 2019, doi: 10.1364/OL.44.003621.
- [52] Y. Li *et al.*, "On-chip zero-index metamaterials," *Nature Photonics*, vol. 9, no. 11, p. 738, 2015.
- [53] X. Huang, Y. Lai, Z. H. Hang, H. Zheng, and C. T. Chan, "Dirac cones induced by accidental degeneracy in photonic crystals and zero-refractive-index materials," *Nature Materials*, vol. 10, p. 582, 05/29/online 2011, doi: 10.1038/nmat3030
<https://www.nature.com/articles/nmat3030#supplementary-information>.
- [54] D. I. Vulis *et al.*, "Monolithic CMOS-compatible zero-index metamaterials," *Optics Express*, vol. 25, no. 11, pp. 12381-12399, 2017/05/29 2017, doi: 10.1364/OE.25.012381.
- [55] O. Reshef, P. Camayd-Muñoz, D. I. Vulis, Y. Li, M. Lončar, and E. Mazur, "Direct Observation of Phase-Free Propagation in a Silicon Waveguide," *ACS Photonics*, vol. 4, no. 10, pp. 2385-2389, 2017.
- [56] X.-T. He *et al.*, "Realization of Zero-Refractive-Index Lens with Ultralow Spherical Aberration," *ACS Photonics*, vol. 3, no. 12, pp. 2262-2267, 2016/12/21 2016, doi: 10.1021/acsp Photonics.6b00714.
- [57] X. Wang, W. Shi, H. Yun, S. Grist, N. A. F. Jaeger, and L. Chrostowski, "Narrow-band waveguide Bragg gratings on SOI wafers with CMOS-compatible fabrication process," *Optics Express*, vol. 20, no. 14, pp. 15547-15558, 2012/07/02 2012, doi: 10.1364/OE.20.015547.
- [58] C. Wang and J. Yao, "Fiber Bragg gratings for microwave photonics subsystems," *Optics Express*, vol. 21, no. 19, pp. 22868-22884, 2013/09/23 2013, doi: 10.1364/OE.21.022868.
- [59] H. Qiu *et al.*, "Silicon band-rejection and band-pass filter based on asymmetric Bragg sidewall gratings in a multimode waveguide," *Optics Letters*, vol. 41, no. 11, pp. 2450-2453, 2016/06/01 2016, doi: 10.1364/OL.41.002450.
- [60] W. Shi *et al.*, "Electrically tunable resonant filters in phase-shifted contra-directional couplers," in *The 9th International Conference on Group IV Photonics (GFP)*, 29-31 Aug. 2012 2012, pp. 78-80, doi: 10.1109/GROUP4.2012.6324092.
- [61] H. Qiu, Y. Su, P. Yu, T. Hu, J. Yang, and X. Jiang, "Compact polarization splitter based on silicon grating-assisted couplers," *Optics Letters*, vol. 40, no. 9, pp. 1885-1887, 2015/05/01 2015, doi: 10.1364/OL.40.001885.
- [62] P. B. Deotare, M. W. McCutcheon, I. W. Frank, M. Khan, and M. Lončar, "High quality factor photonic crystal nanobeam cavities," *Applied Physics Letters*, vol. 94, no. 12, p. 121106, 2009, doi: 10.1063/1.3107263.
- [63] Y. A. Vlasov, M. O'Boyle, H. F. Hamann, and S. J. McNab, "Active control of slow light on a chip with photonic crystal waveguides," *Nature*, vol. 438, no. 7064, pp. 65-69, 2005/11/01 2005, doi: 10.1038/nature04210.
- [64] Z. Huang *et al.*, "Strong Optomechanical Coupling in Nanobeam Cavities based on Hetero Optomechanical Crystals," *Scientific Reports*, Article vol. 5, p. 15964, 11/04/online 2015, doi: 10.1038/srep15964.
- [65] Y. Li *et al.*, "Optomechanical crystal nanobeam cavity with high optomechanical coupling rate," *Journal of Optics*, vol. 17, no. 4, p. 045001, 2015/02/26 2015, doi: 10.1088/2040-8978/17/4/045001.
- [66] B. Qi, P. Yu, Y. Li, X. Jiang, M. Yang, and J. Yang, "Analysis of Electrooptic Modulator With 1-D Slotted Photonic Crystal Nanobeam Cavity," *IEEE Photonics Technology Letters*, vol. 23, no. 14, pp. 992-994, 2011, doi: 10.1109/LPT.2011.2148704.
- [67] J. Hendrickson, R. Soref, J. Sweet, and W. Buchwald, "Ultrasensitive silicon photonic-crystal nanobeam electro-optical modulator: Design and simulation," *Optics Express*, vol. 22, no. 3, pp. 3271-3283, 2014/02/10 2014, doi: 10.1364/OE.22.003271.
- [68] Q. Quan, P. B. Deotare, and M. Loncar, "Photonic crystal nanobeam cavity strongly coupled to the feeding waveguide," *Applied Physics Letters*, vol. 96, no. 20, p. 203102, 2010, doi: 10.1063/1.3429125.
- [69] T. F. Krauss, R. M. D. L. Rue, and S. Brand, "Two-dimensional photonic-bandgap structures operating at near-infrared wavelengths," *Nature*, vol. 383, no. 6602, pp. 699-702, 1996/10/01 1996, doi: 10.1038/383699a0.
- [70] S.-Y. Lin, E. Chow, V. Hietala, P. R. Villeneuve, and J. D. Joannopoulos, "Experimental Demonstration of Guiding and Bending of Electromagnetic Waves in a Photonic Crystal," *Science*, vol. 282, no. 5387, pp. 274-276, 1998, doi: 10.1126/science.282.5387.274.
- [71] P. Cheben *et al.*, "Broadband polarization independent nanophotonic coupler for silicon waveguides with ultra-high efficiency," *Optics Express*, vol. 23, no. 17, pp. 22553-22563, 2015/08/24 2015, doi: 10.1364/OE.23.022553.
- [72] M. Zadka, U. D. Dave, and M. Lipson, "High Tolerance of Metamaterial Waveguides to Fabrication Variations," in *Conference on Lasers and Electro-Optics*, San Jose, California, 2019/05/05 2019: Optical Society of America, in OSA Technical Digest, p. SF1J.7, doi: 10.1364/CLEO_SI.2019.SF1J.7. [Online]. Available: http://www.osapublishing.org/abstract.cfm?URI=CLEO_SI-2019-SF1J.7
- [73] A. Ortega-Moñux *et al.*, "Disorder effects in subwavelength grating metamaterial waveguides," *Optics Express*, vol. 25, no. 11, pp. 12222-12236, 2017/05/29 2017, doi: 10.1364/OE.25.012222.
- [74] V. R. Almeida, Q. Xu, C. A. Barrios, and M. Lipson, "Guiding and confining light in void nanostructure," *Optics Letters*, vol. 29, no. 11, pp. 1209-1211, 2004/06/01 2004, doi: 10.1364/OL.29.001209.
- [75] A. Sánchez-Postigo *et al.*, "Mid-infrared suspended waveguide platform and building blocks," *IET Optoelectronics*, vol. 13, no. 2, pp. 55-61, 2019, doi: 10.1049/iet-opt.2018.5067.
- [76] W. Zhou, Z. Cheng, X. Wu, X. Sun, and H. K. Tsang, "Fully suspended slot waveguide platform," *Journal of Applied Physics*, vol. 123, no. 6, p. 063103, 2018/02/14 2018, doi: 10.1063/1.5017780.
- [77] L. B. Soldano and E. C. Pennings, "Optical multi-mode interference devices based on self-imaging: principles and applications," *Journal of lightwave technology*, vol. 13, no. 4, pp. 615-627, 1995.
- [78] R. Halir *et al.*, "Ultra-broadband nanophotonic beamsplitter using an anisotropic sub-wavelength metamaterial," *Laser & Photonics Reviews*, vol. 10, no. 6, pp. 1039-1046, 2016, doi: 10.1002/lpor.201600213.
- [79] A. H. Bermello, J. M. L. Gonzalez, A. Velasco, A. Ortega-Monux, P. Cheben, and R. Halir, "Design of a broadband polarization splitter based on anisotropy-engineered tilted subwavelength gratings," *IEEE Photonics Journal*, 2019.
- [80] A. Zanzi, A. Brimont, A. Griol, P. Sanchis, and J. Marti, "Compact and low-loss asymmetrical multimode interference splitter for power monitoring applications," *Optics letters*, vol. 41, no. 2, pp. 227-229, 2016.
- [81] Y. D'Mello *et al.*, "Compact, Angled Polarization Splitter: Characterization of Broadband Performance and Fabrication Tolerance," *IEEE Photonics Journal*, vol. 10, no. 6, pp. 1-12, 2018, doi: 10.1109/JPHOT.2018.2878905.
- [82] Y. Shi, D. Dai, and S. He, "Proposal for an ultracompact polarization-beam splitter based on a photonic-crystal-assisted multimode interference coupler," *IEEE Photonics Technology Letters*, vol. 19, no. 11, pp. 825-827, 2007.
- [83] L. Xu *et al.*, "Compact Broadband Polarization Beam Splitter Based on Multimode Interference Coupler With Internal

- Photonic Crystal for the SOI Platform," *Journal of Lightwave Technology*, vol. 37, no. 4, pp. 1231-1240, 2019.
- [84] Y. Wang *et al.*, "Ultra-Compact Sub-Wavelength Grating Polarization Splitter-Rotator for Silicon-on-Insulator Platform," *IEEE Photonics Journal*, vol. 8, no. 6, pp. 1-9, 2016, doi: 10.1109/JPHOT.2016.2630849.
- [85] Y. Xu and J. Xiao, "Ultracompact and high efficient silicon-based polarization splitter-rotator using a partially-etched subwavelength grating coupler," *Scientific reports*, vol. 6, p. 27949, 2016.
- [86] D. Zhao, J. Zhang, P. Yao, X. Jiang, and X. Chen, "Photonic crystal Mach-Zehnder interferometer based on self-collimation," *Applied Physics Letters*, vol. 90, no. 23, p. 231114, 2007/06/04 2007, doi: 10.1063/1.2746942.
- [87] K. McGarvey-Lechable and P. Bianucci, "Bloch-Floquet Waves in Optical Ring Resonators," in *Conference on Lasers and Electro-Optics*, San Jose, California, 2019/05/05 2019: Optical Society of America, in OSA Technical Digest, p. SW4J.2, doi: 10.1364/CLEO_SI.2019.SW4J.2. [Online]. Available: http://www.osapublishing.org/abstract.cfm?URI=CLEO_SI-2019-SW4J.2
- [88] M. Soljačić, S. G. Johnson, S. Fan, M. Ibanescu, E. Ippen, and J. D. Joannopoulos, "Photonic-crystal slow-light enhancement of nonlinear phase sensitivity," *J. Opt. Soc. Am. B*, vol. 19, no. 9, pp. 2052-2059, 2002/09/01 2002, doi: 10.1364/JOSAB.19.002052.
- [89] J. Gonzalo Wangüemert-Pérez *et al.*, "Evanescent field waveguide sensing with subwavelength grating structures in silicon-on-insulator," *Optics Letters*, vol. 39, no. 15, pp. 4442-4445, 2014/08/01 2014, doi: 10.1364/OL.39.004442.
- [90] J. Upham, B. Gao, L. O'Faolain, Z. Shi, S. A. Schulz, and R. W. Boyd, "Realization of a flat-band superprism on-chip from parallelogram lattice photonic crystals," *Optics Letters*, vol. 43, no. 20, pp. 4981-4984, 2018/10/15 2018, doi: 10.1364/OL.43.004981.
- [91] J. Moon *et al.*, "Continuous Wave Green Lasing at Room Temperature in Two-Dimensional Photonic Crystal Perovskite Laser," in *Conference on Lasers and Electro-Optics*, San Jose, California, 2019/05/05 2019: Optical Society of America, in OSA Technical Digest, p. SW4N.2, doi: 10.1364/CLEO_SI.2019.SW4N.2. [Online]. Available: http://www.osapublishing.org/abstract.cfm?URI=CLEO_SI-2019-SW4N.2
- [92] B. Jalali, "Making Silicon Lase," *Scientific American*, vol. 296, no. 2, pp. 58-65, Feb 2007. [Online]. Available: <http://www.jstor.org/stable/26069154>.
- [93] P. Tréguer *et al.*, "Influence of diatom diversity on the ocean biological carbon pump," *Nature Geoscience*, vol. 11, no. 1, pp. 27-37, 2018/01/01 2018, doi: 10.1038/s41561-017-0028-x.
- [94] P. Kuczynska, M. Jemiola-Rzeminska, and K. Strzalka, "Photosynthetic pigments in diatoms," *Marine drugs*, vol. 13, no. 9, pp. 5847-5881, 2015.
- [95] Y. D'Mello, D. Petrescu, J. Skoric, M. Campbell, M. Andrews, and D. V. Plant, "Characterization of the Photonic Response in *Nitzschia Filiformis* Phytoplankton," in *Conference on Lasers and Electro-Optics (CLEO)*, San Jose, 2018: OSA, pp. 1-2.
- [96] T. Fuhrmann, S. Landwehr, M. El Rharbi-Kucki, and M. Sumper, "Diatoms as living photonic crystals," *Applied Physics B*, vol. 78, no. 3-4, pp. 257-260, 2004.
- [97] Y. D'Mello, S. Bernal, J. Skoric, D. Petrescu, M. Andrews, and D. V. Plant, "Photonic Crystal Behavior of *Nitzschia Filiformis* Phytoplankton for Chlorophyll A Photosynthesis," in *Conference on Lasers and Electro-Optics (CLEO)*, San Jose, 2019: OSA.
- [98] M. Taniguchi and J. S. Lindsey, "Database of Absorption and Fluorescence Spectra of > 300 Common Compounds for use in Photochem CAD," *Photochemistry and photobiology*, vol. 94, no. 2, pp. 290-327, 2018.
- [99] C. Liu, M. Rybin, P. Mao, S. Zhang, and Y. Kivshar, "Disorder-Immune Photonics Based on Mie-Resonant Dielectric Metamaterials," in *Conference on Lasers and Electro-Optics*, San Jose, California, 2019/05/05 2019: Optical Society of America, in OSA Technical Digest, p. FF3B.6, doi: 10.1364/CLEO_QELS.2019.FF3B.6. [Online]. Available: http://www.osapublishing.org/abstract.cfm?URI=CLEO_QE-LS-2019-FF3B.6
- [100] T. Dbouk, "A review about the engineering design of optimal heat transfer systems using topology optimization," *Applied Thermal Engineering*, vol. 112, pp. 841-854, 2017/02/05/ 2017, doi: <https://doi.org/10.1016/j.applthermaleng.2016.10.134>.
- [101] J.-H. Zhu, W.-H. Zhang, and L. Xia, "Topology Optimization in Aircraft and Aerospace Structures Design," *Archives of Computational Methods in Engineering*, vol. 23, no. 4, pp. 595-622, 2016/12/01 2016, doi: 10.1007/s11831-015-9151-2.
- [102] J. Lu and J. Vučković, "Nanophotonic computational design," *Optics express*, vol. 21, no. 11, pp. 13351-13367, 2013.
- [103] M. H. Tahersima *et al.*, "Deep Neural Network Inverse Design of Integrated Photonic Power Splitters," *Scientific Reports*, vol. 9, no. 1, p. 1368, 2019/02/04 2019, doi: 10.1038/s41598-018-37952-2.
- [104] B. Shen, P. Wang, R. Polson, and R. Menon, "An integrated-nanophotonics polarization beamsplitter with $2.4 \times 2.4 \mu\text{m}^2$ footprint," *Nature Photonics*, vol. 9, no. 6, p. 378, 2015.